JOURNAL OF SPACECRAFT AND ROCKETS
Vol. 49, No. 1, January–February 2012

Linear Stability Analysis of Nose Bluntness Effects on Hypersonic Boundary Layer Transition

Jia Lei* and Xiaolin Zhong†
University of California, Los Angeles, California 90095

DOI: 10.2514/1.52616

For hypersonic flow over spherical cones of small nose radii, it has been experimentally observed and theoretically explained that the nose bluntness effect leads to a delay of boundary-layer transition. In contrast, this trend reverses when the nose radii are larger than some critical values in the large nose bluntness range. This transition reversal phenomenon was mainly reported in Stetson and Rushton's transition experiments of a Mach 5.5 flow [1] and Softley's Mach 10–12 experiments [2] in 1967. Several linear stability analyses have been performed since the 1990s to study the nose bluntness effects on transition; none were able to show the reversal of instability onset due to nose blunting. All of the previous stability analyses, however, suffered from the fact that they were conducted only on test cases in which the actual transition reversal was not experimentally observed. The objective of the current study is to conduct a linear stability analysis on Stetson and Rushton's Mach 5.5 experiments in which the reversal is observed. Three cones with nose radii of 0.156, 0.5, and 1.5 in., covering both the small and large bluntness regions, are used to study the effect of nose bluntness on stability and transition. It is found that, if only the second-mode instabilities are considered, the onset of instability is always delayed as the nose bluntness increases. The linear stability theory calculations show no reversal on the growth of the second-mode instability.

Nomenclature

a	=	nondimensional wave speed
e	=	total energy per unit volume, J/m^3
F	=	frequency, Hz
F_i	=	inviscid flux vector
F_v	=	viscous flux vector
L	=	boundary-layer characteristic length scale, m
M	=	Mach number
N	=	N factor
P	=	pressure, N/m^2
Pr	=	Prandtl number
R	=	local Reynolds number
Re_n	=	Reynolds number based on the nose radius
Re_∞	=	freestream unit Reynolds number, 1/m
R_n	=	nose radius, mm
s	=	distance along the cone surface from the nose tip, m
T	=	temperature, K
T_w	=	temperature at the cone surface, K
u, v, w	=	velocity components, m/s
x_1, x_2, x_3	=	Cartesian coordinate in physical space
y_n	=	normalized local normal distance from cone surface
α_i^*	=	growth rate, 1/m
α_r^*	=	streamwise wave number, 1/m
γ	=	ratio of specific heats
θ	=	cone half angle, °
μ	=	viscosity, kg/m-s
ξ, η, ς	=	coordinates in transformed space
ρ	=	density, kg/m^3
τ	=	shear stress, N/m^2
ϕ	=	phase angular, rad
ω	=	angular frequency, rad/s

Superscript

$*$	=	dimensional quantity

Subscript

r, i	=	real/imaginary part of a complex number
∞	=	freestream quantity

Presented as Paper 2010-0898 at the 48th AIAA Aerospace Sciences Meeting including the New Horizons Forum and Aerospace Exposition, Orlando, FL, 4–7 January 2010; received 1 October 2010; revision received 20 July 2011, accepted for publication 23 August 2011.

*Graduate Student, Mechanical and Aerospace Engineering Department; jxlei@ucla.edu. Student Member AIAA (Corresponding Author).

†Professor, Mechanical and Aerospace Engineering Department; xiaolin@seas.ucla.edu. Associate Fellow AIAA.

I. Introduction

FOR hypersonic flow over blunt cones, it has been experimentally observed [3] and theoretically explained [4] that the location of laminar-turbulent transition moves downstream when the nose radii increase within the small bluntness region. This trend is reversed when the nose radii are larger than some certain critical values based on experimental observations [1,2]. This phenomenon is known as transition reversal due to nose bluntness. In other words, increasing the nose radius beyond the critical value leads to an upstream movement of the location of transition. The downstream movement of the transition location at small radii can be explained by the reduction of local Reynolds numbers owing to the entropy layer created by nose bluntness. However, there is still no satisfactory explanation for the cause of the transition reversal at large nose bluntness.

Most of the previous studies of bluntness effects on transition were based on linear stability analysis, performed on Stetson et al.'s stability experiments of an axisymmetric blunt cone in a Mach 7.99 flow [5]. In these experiments, detailed fluctuation spectra were documented for disturbance waves developing along the body surface. The freestream unit Reynolds number per foot was 2.68×10^6. The experimental results showed that disturbances in the boundary layer were dominated by second-mode instability. Significant super harmonic components of the second mode were also observed after the second mode became dominant. The cone models used in the experiments were not long enough for transition to occur in the boundary layer. As a result, the transition reversal phenomenon was not observed in these experiments. Compared with hypersonic flow over a sharp cone, second-mode instability of the blunt cones

appeared at locations much further downstream, indicating a stabilization of the boundary layer by small nose bluntness.

Linear stability characteristics of the boundary-layer flow over the same blunt cone used in Stetson et al.'s experiments have been studied by a number of researchers [4,6–9]. Malik et al. [4] computed the neutral stability curve and compared the growth rates obtained from linear stability theory (LST) with the experimental results. The steady base flow solution was computed using the parabolized Navier-Stokes equations. The results showed that the nose-blunting effect stabilizes the boundary layer. The linear stability analyses predicted a slightly lower frequency for the dominant second mode but much higher amplification rates than the experimental results. Rosenboom et al. [9] did a further linear stability study on the effect of nose bluntness on hypersonic boundary-layer stability. In their calculations, the cone geometry and flow conditions were the same as those used in the Stetson et al.'s Mach 7.99 experiments. Three cases of blunt cones with different nose radii, covering both small and large bluntness, were considered. The purpose was to investigate the transition reversal phenomenon at large bluntness. By a linear stability analysis, Rosenboom et al. confirmed a monotonic downstream movement of the second-mode critical Reynolds number as the nose radius increases. Their LST results did not show the transition reversal phenomenon observed in experiments at large bluntness.

Zhong [10,11] and Zhong and Ma [12] conducted numerical simulations on the stability and receptivity of the same Stetson et al's Mach 7.99 flow over blunt cones. In Zhong and Ma [12], numerical results for the steady base flow were compared with the experimental results of Stetson and Rushton [1] and the numerical results of Esfahanian [13]. In addition, a normal-mode linear stability analysis was used to identify the main components of boundary-layer disturbances generated by forcing freestream fast acoustic waves. It was found that neither the first-mode nor the second-mode instability waves are excited directly by freestream fast acoustic waves in the early region along the cone surface, although the Mack modes can be unstable. Instead, the second mode is excited downstream of the second-mode branch I neutral stability point. The delay of the second-mode excitation is a result of the fact that the hypersonic boundary-layer receptivity is governed by a two-step resonant interaction process: 1) resonant interactions between the forcing waves and a stable boundary-layer wave mode I near the leading edge region and 2) resonant interactions between the induced stable mode I and the unstable second Mack mode downstream.

Zhong [11] conducted a numerical study on the effects of nose bluntness on the receptivity to freestream acoustic waves for hypersonic flow by comparing the results of three nose radii. The flow conditions duplicated the experiments of Stetson et al. [5]. They investigated the effects of nose bluntness on receptivity. Three nose radii were chosen to be the same as those used in Rosenboom et al.'s stability analysis [9]: 0.15, 0.5, and 1.5 in. The first nose radius belonged to the category of small nose bluntness, whereas the second and third cases fell into the region of large bluntness. It was found that, in those three test cases, the basic receptivity mechanism of hypersonic flow over the blunt cone with different nose radii is essentially the same. Specifically, the receptivity is a result of the resonant interaction between forcing waves and boundary-layer wave modes near the nose region and the resonant interaction between different boundary-layer wave modes downstream.

Transition delay due to small nose bluntness can be explained by the reduction of local Reynolds numbers due to the entropy layer created by the bow shock. On the other hand, the mechanisms of transition reversal for cones with larger bluntness have not been fully understood. So far, LST and numerical-simulation studies on blunt-cone effects have been done mainly on the test cases of Stetson et al.'s Mach 7.99 experiment [5]. However, Stetson et al's Mach 7.99 test model was not long enough to observe transition experimentally. In other words, the transition reversal phenomenon was not actually observed in Stetson et al.'s Mach 7.99 cases. Even though all of the previous LST and simulation studies on Stetson et al.'s Mach 7.99 case provided a solid understanding of the nose-blunting effect in the delay of transition, Stetson et al.'s Mach 7.99 case is not a good candidate for analyzing the reversal mechanism. A more direct way to gain insight into the reversal in transition is to study a case in which the actual reversal was observed experimentally.

Though the delay of transition by slight nose blunting has been found in many experiments, the transition reversals at large nose bluntness have only been reported in a few experiments. The authors can find only two publications on experiments for which the transition reversals were found. Stetson and Rushton [1] were the first ones to report concrete results on transition reversal. The only other source where reversal results were reported was from Softley [2] on a set of Mach 10–12 flows over blunt cones with a half angle of 5°.

Extensive experimental data on transition and transition reversal were reported by Stetson and Rushton for Mach 5.5 flow over sharp and blunt cones [1]. Blunt cones, with nose radii ranging from $1/32$ to 1 and $1/2$ in., were tested, and the transition locations were measured. Transition data obtained in these test models is replotted in Fig. 1 (left), which shows the transitional Reynolds numbers vs freestream Reynolds numbers based on nose radii, Re_n. The figure shows a clear transition reversal as Re_n increases, with 2×10^5 as the dividing line between large and small nose radii for Re_n. These results have a very similar trend to the transition reversal results of Softley [2], collected from Mach 10–12 flows over a set of small and large blunt cones, as shown in Fig. 1 (right).

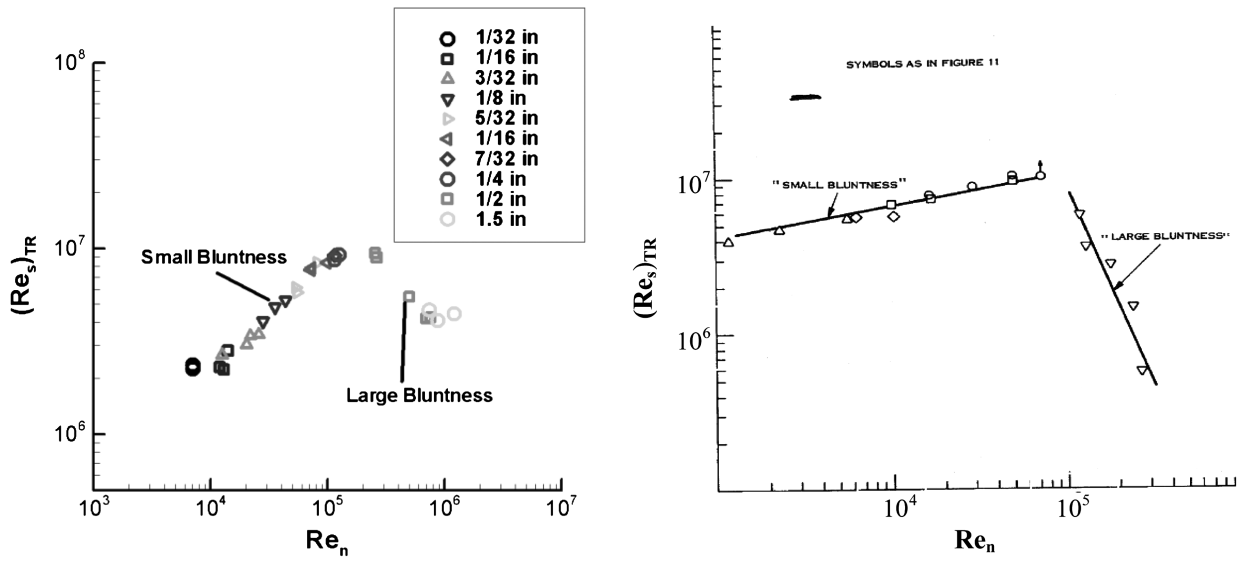

Fig. 1 Transition Reynolds number vs Reynolds number based on nose radius reported by Stetson and Rushton (left) [1] and Softley [2] (right).

Even though many studies have been done on the blunt-nose effect on hypersonic boundary-layer transition, there have not been any reported LST studies on either Stetson and Rushton's Mach 5.5 experiment [1] or Softley's Mach 10–12 experiments [2], which are among the few experimental test cases that actually show transition reversal. It will be valuable if these experiments can be systematically reanalyzed by modern simulation and linear stability techniques to study the effects of nose bluntness on transition. The experimental measurements on the parametric effects on transition can be correlated with the LST results to identify the instability mechanisms. Therefore, the objective of this paper is to conduct LST studies of Stetson and Rushton's Mach 5.5 case to explore the nose bluntness effects to the transition. To verify the LST results, two test cases of numerical simulation of the same boundary-layer flow induced by wall blowing and suction are performed. The simulation results are compared with the corresponding LST results for the mode structures, wave speeds, and growth rates. In this paper, LST results are presented on three test cases of 0.156, 0.5, and 1.5 in. nose radii. The simulation of hypersonic flows over blunt cones corresponds to the flow conditions of Stetson and Rushton's Mach 5.5 experiment. Following that, the range of unstable second-mode frequencies are identified for each case by LST studies, which are then used as the forcing frequencies in the unsteady simulations to validate the LST study. Also, the second-mode N factors are computed using the disturbance waves from which the growth rates are obtained. The N factors are then used to compare the predicted transition location to the transition location reported in the experiment.

II. Governing Equations and Numerical Method

The governing equations are the unsteady compressible three-dimensional (3-D) Navier-Stokes equations. The advantage of solving the full Navier-Stokes equations is that they contain the least amount of approximation such that, if implement correctly, they can resolve the flowfield with very high accuracy. The Navier-Stokes equations can be written in the following conservative form:

$$\frac{\partial U^*}{\partial t^*} + \frac{\partial F_j^*}{\partial x_j^*} + \frac{\partial F_{vj}^*}{\partial x_j^*} = 0 \tag{1}$$

where $U* = (\rho^*, \rho^* u_1^*, \rho^* u_2^*, \rho^* u_3^*, e^*)$, and the F^* terms are flux terms that can be expanded as

$$F_j^* = \begin{Bmatrix} \rho u_j \\ \rho u_{j1} u_j + p\delta_{1j} \\ \rho u_{j2} u_j + p\delta_{1j} \\ \rho u_{j3} u_j + p\delta_{1j} \\ (e+p)u_j \end{Bmatrix} \quad \text{and} \quad F_{vj}^* = \begin{Bmatrix} 0 \\ \tau_{1j} \\ \tau_{2j} \\ \tau_{3j} \\ \tau_{jk} u_k - q_j \end{Bmatrix} \tag{2}$$

The Cartesian coordinates, (x^*, y^*, z^*), are denoted in index notation. In the current simulation of axisymmetric flow over blunt cones, x^* is the coordinate along the centerline of the cone pointing toward the downstream direction. The origin of the coordinates is collocated with the center of the spherical nose. Grid transformation is used to transform the body-fitted stretched grids in the Cartesian coordinates, (x^*, y^*, z^*), into uniform grids in the computational domain, (ξ, η, ς). Figure 2 shows the two-dimensional (2-D) mesh of the current computational case 2 near the leading edge of the cone with two sets of coordinate systems labeled.

A. Steady Base Flow

The laminar mean flow solution needs to be obtained to serve as the base flow for the LST analysis. A fifth-order shock-fitting method developed by Zhong [14] is used to compute the flowfield bounded by the bow shock and cone surface. The shock-fitting method treats the shock as the computational boundary to avoid jumps and discontinuities in the flowfield. The flow variables right behind the shock are determined by Rakine-Hugoniot relations across the shock and the characteristic compatibility equations. The flowfield in the computational domain is approximated using a high-order upwind finite difference scheme with an adjustable artificial viscosity coefficient. Because the performance of the linear stability analysis is very sensitive to the base flow solution, the base flow must have high accuracy in order to obtain reliable stability results. The shock-fitting scheme developed by our research group at UCLA has been tested and proven to be accurate and reliable by a number of previous studies [12,15,16].

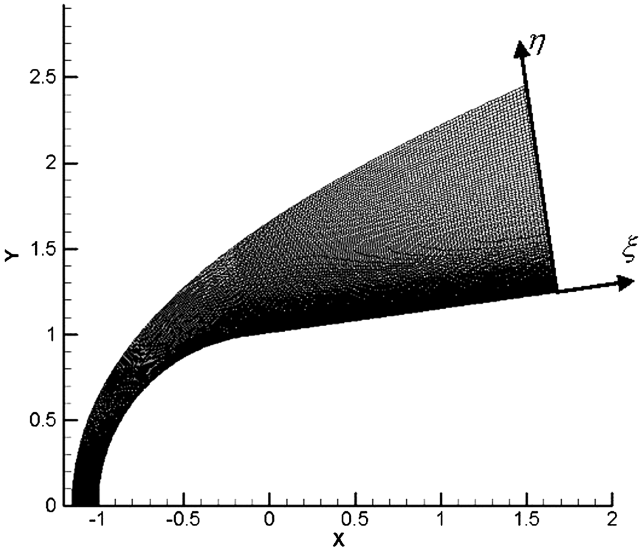

Fig. 2 Schematic of 2-D grid for case 1 near the leading edge.

B. Linear Stability Theory

LST is used to study the instability modes in the boundary layer of hypersonic flow over blunt cones in this paper. To apply LST, the disturbance amplitudes are assumed to be small enough so that they do not interact nonlinearly with each other. The normal mode of a disturbance is assumed to have the following form:

$$q' = \hat{q}(y_n) e^{i(-\omega t + \alpha s)} \tag{3}$$

where q' can be any dimensionless flow variable, such as velocity, temperature, density, and pressure, all of which are normalized by the freestream quantities. $\hat{q}$ is the mode structure representing the complex amplitude of the disturbance. In the spatial stability theory, ω, the dimensionless angular frequency of a normal disturbance mode, is set to be a real number. $\alpha = \alpha_r + i\alpha_i$ is the streamwise complex wave number nondimensionalized by L^*. The imaginary part of the wave number represents the spatial growth rate of a specific disturbance mode. When α_i is negative, the disturbance becomes unstable. The real part of the wave number, α_r, indicates the spatial wave number. An important quantity that can be extracted from α_r is the nondimensional phase velocity, which is defined as

$$a = \frac{\omega}{\alpha_r} = \frac{FR}{\alpha_r} \tag{4}$$

In the preceding equation, the dimensionless phase velocity, a, is normalized by the freestream velocity. F is the dimensionless frequency that is related to the dimensional angular frequency by

$$F = \frac{\omega^* \upsilon_\infty^*}{u_\infty^{*2}} \tag{5}$$

R is local Reynolds number based on the length scale of boundary-layer thickness, and s^* is the curvilinear coordinate along the cone surface as measured from the nose.

$$R = \frac{\rho_\infty^* u_\infty^* L^*}{\mu_\infty^*} \tag{6}$$

$$L^* = \sqrt{\frac{\mu^*_\infty s^*}{\rho^*_\infty U^*_\infty}} \tag{7}$$

One of the most common applications of LST analysis in predicting the laminar-turbulent transition is to calculate the N factor based on a semi-empirical method called the e^N method. According to the theory, when the amplification of the disturbances reaches certain levels, transition will occur. The ratio of the amplitude of disturbance waves with a fixed frequency can be calculated as they travel downstream. Because the growth rate varies from location to location, the amplitude ratio between two locations can be expressed as the following integral:

$$e^N = \frac{A}{A_0} = \exp \int_{s^*_0}^{s^*} \frac{1}{A}\frac{\mathrm{d}A}{\mathrm{d}s}\,\mathrm{d}s^* \tag{8}$$

or, just for the N factor,

$$N = \int_{s^*_0}^{s^*} -\alpha^*_i\,\mathrm{d}s^* \tag{9}$$

In Eq. (8), s^*_0 corresponds to the location where the disturbance becomes neutrally stable (or the branch I instability point). By computing this integral, we know how much the amplitude for a specific disturbance changes as it moves downstream. On the other hand, the N factor leading to transition is correlated to the experimental measurement. The N factor is not unique for all cases; it depends on the flow conditions, object geometry, amplitude of freestream disturbance, and other unknown parameters. Even in one single case, the N factor differs when different unstable modes are considered. Here, the different unstable modes refer to the first mode and the second mode introduced by Mack [17]. In general, the N factor for the first mode is smaller than the one for the second mode. It should be noted the main focus of this paper is the stability and N-factor calculations of the 2-D (axisymmetric) second mode for the current test case. Even though the 3-D first-mode instability is responsible for the transition at a lower Mach number flow, extensive theoretical analysis, numerical simulations, and experiments have shown that, for higher Mach number flows ($M > 4$), the axisymmetric second-mode instability is the most dominant unstable mechanism in the hypersonic boundary layer [18,19]. In the current cases, because a cool-wall boundary condition is enforced, the first mode is stabilized as being proven theoretically [17,20]. As discussed later in this paper, the first mode instability is not found in all three cases considered in this study due to the wall-cooling effect. Therefore, the current paper only focuses on the second-mode instability, which is most amplified when the disturbance is axisymmetric [4,17].

C. LST Code Validations

The current LST code is developed based on Malik's multidomain spectral collocation method formulations published in 1990 [21]. The LST code formulates the linear stability model into an eigen problem in which the eigenvalue represents the spatial growth rate of the normal mode, and the eigenvector is the mode shape of the normal mode. Because of the fact that the flowfield is not self-similar, especially in the region close the nose, the LST code marches down the base flow profiles station by station to obtain the local growth rate and the mode structure of the normal mode at the desired frequency.

To verify the reliability of the LST code developed, two validation cases are presented. The first case is Stetson et al.'s Mach 7.99 flow over a blunt cone with a nose radius of 0.1 in. and a half angle of 7° [5]. This case has been studied by many other researchers, making it an ideal validation case. Figure 3 shows the current LST second-mode growth rate compared with the growth rates from Malik et al. [4] and Esfahanian [13]. α_i is the nondimensional growth rate and ω is the nondimensional angular frequency. The growth rate is calculated at a fixed cone location 150 times the nose radius ($s = 150$) downstream of the nose tip. In the figure, the current result

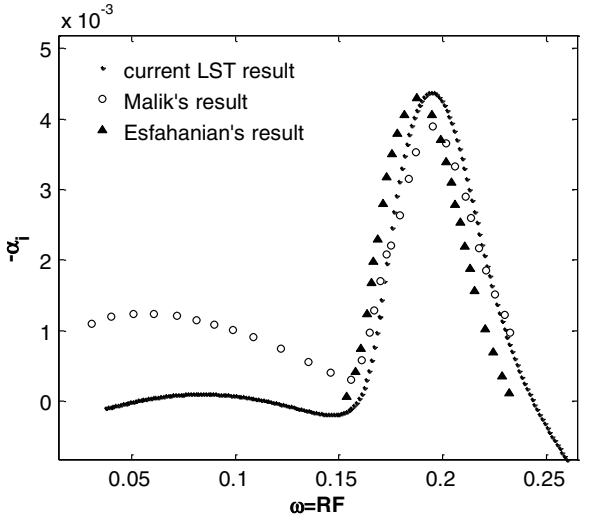

Fig. 3 Comparison of unstable mode growth rates calculated by different researchers.

compares reasonably well to the other researchers' in the second-mode region where ω is greater than 0.15. The slight discrepancy is mainly due to the variations in steady flow calculations by different numerical schemes and flow models [4,13]. However, in the first-mode region, the current result looks to be substantially lower than Malik's result because, in the current LST calculation, only the axisymmetric waves are considered, whereas in Malik's result, the maximum growth rate obtained from oblique wave angles was presented.

The second validation case is the Mach 6 flow over a blunt-nose compression cone designed by Wheaton et al. at Purdue University [18]. In their paper, the N factor was reported, and the unstable second mode was identified based on an LST study on a cone with a blunt nose of 1 mm in radius. The LST results were found to agree well with their experimental measurements. In the current LST study, a consistent N factor result is reproduced with the base flow data from Huang and Zhong [22]. Figure 4 shows the comparison of N factor calculations from Wheaton et al. with the one from the current LST analysis at a single frequency of 297.50 kHz. The results agree well on both the instability wave onset location and amplification factors at different locations. The current result shows a slightly higher N factor than the one from Wheaton et al. This primarily can be explained by the fact that, in our result, the base flow is calculated using a fifth-order shock-fitting scheme, whereas the base flow from Wheaton et al. is generated using a high-order shock-capturing method that has less resolution at the shock. In addition, there are also

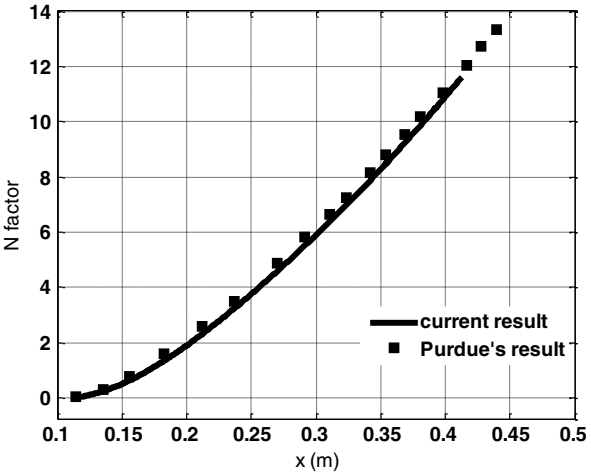

Fig. 4 Comparison of the N factor of the second mode of Mach 6 compression cone presented by Wheaton et al. [18].

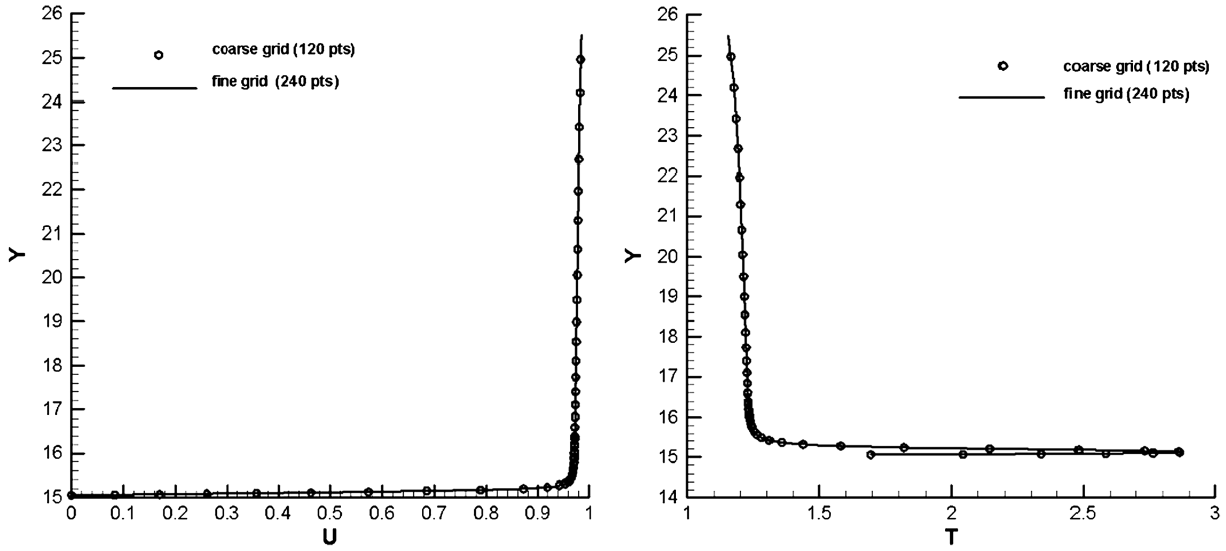

Fig. 5 Comparison of U velocity and temperature profiles for two sets of grids.

plausible differences in the LST model between our code and Wheaton et al.'s. For example, the curvature effect in the streamwise direction is not considered in our LST model. Because the detail for their LST model was not provided in Wheaton et al.'s paper, it is impossible to further investigate the source of this discrepancy.

III. Test Cases and Flow Conditions

A. Test Cases

The flow conditions for the current test case studied in this paper are the same as those in Stetson and Rushton's experiments on a Mach 5.5 air flow over blunt cones [1] where actual transition reversals had been observed. For the case of zero angle of attack, Stetson and Rushton tested 10 blunt cones of different nose radii, ranging from $1/32$ in to 1 and $1/2$ in. Flows with different freestream unit Reynolds numbers ranging from $1.6 \times 10^6/\text{ft}$ to $18 \times 10^6/\text{ft}$ were used. In this paper, cones of three different nose radii with the same freestream flow conditions are chosen. The nose radii of the three cases are:

$$\text{case 1:} r_n = 1.5 \text{ in} = 38.1 \text{ mm}, \qquad \text{Re}_n = 721,995$$

$$\text{case2:} r_n = 0.5 \text{ in} = 12.7 \text{ mm}, \qquad \text{Re}_n = 240,665$$

$$\text{case3:} r_n = 0.156 \text{ in} = 3.969 \text{ mm}, \qquad \text{Re}_n = 75,213$$

The third case, with a nose radius of 0.156 in., falls into the category of small bluntness based on its nose Reynolds number (Re_n). The first and second cases, according to Stetson and Rushton's criteria, fall into the category of large nose bluntness, where the reversals were observed as shown in Fig. 1 (left).

B. Flow Freestream Conditions

The actual flow conditions used in the numerical simulation, which are the same for all three cases, are shown in Table 1. Sutherland's law of viscosity is adopted to calculate the local viscosity based on the local temperature. In the current study, for the steady base flow, the freestream angle of attack is set to zero.

C. Boundary Conditions

For the steady base flow simulation, the inflow and the upper computation boundary are bounded by the bow shock with the freestream conditions applied right outside the shock wave. On the cone surface, nonslipped boundary conditions are enforced on the velocity vector. The wall temperature is set to be at a constant, which is equal to the room temperature of 296 K. The pressure at the wall is obtained using high-order extrapolation, and the density can be calculated by perfect gas equation. At the outflow, a high-order polynomial extrapolation is used to obtain the flow quantities at the exit of computational domain.

IV. Simulation Results of The Steady Base Flows

As mentioned in the preceding section, the steady base flows are computed using a fifth-order shock-fitting scheme with a multiple zones approach. In the computational domain, the wall normal direction is resolved using 240 grid points with stretching toward the cone surface to ensure that there is approximately 100 grid points within the boundary layer. Because the computational fluid dynamics code is designed with 3-D geometry in mind, four points are used in the transverse direction to enforce the axisymmetric flow configuration. However, in the actual computation, only one point is actually being calculated. The simulations are carried out up to 0.8 m, 1.8 m, and 3.2 m along the cone surfaces for the cases with nose radii

Table 1 Flow conditions and parameters of current cases

$M_\infty = 5.468$	$P^*_\infty = 7756.56$ Pa	$T^*_\infty = 174.46$ K	$Re_\infty = 18.95 \times 10^6 \text{m}^{-1}$
$T_{\text{wall}} = 296\text{K}$	$\gamma = 1.4$	$Pr = 0.72$	cone half angle $= 8°$

Table 2 Computational grid points of steady base flows

Nose radius	Grids in wall normal direction, η	Grids in streamwise direction, ξ	Streamwise length, s	Grids in transverse direction, ς
0.156 in.	240	4440	0.8 m	4
0.5 in.	240	4800	1.8 m	4
1.5 in.	240	4800	3.2 m	4

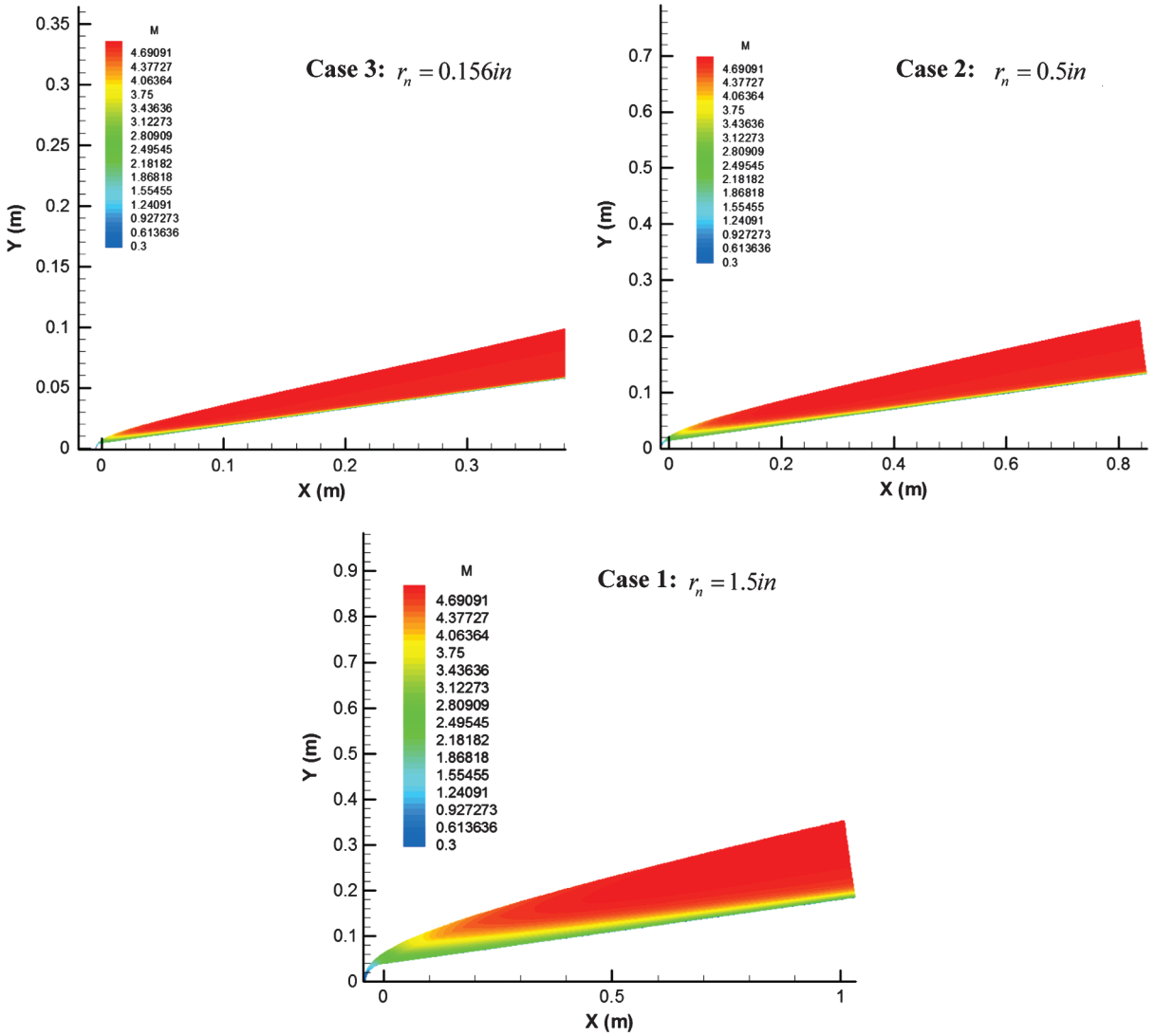

Fig. 6 Mach number contours of the three test cases of different nose radii.

of 0.156, 0.5, and 1.5 in., respectively. The number of grid points per unit length in the streamwise direction is intentionally reduced as the nose bluntness increases for the reason that the flow gradient in the streamwise direction is not as large as in the wall normal direction, with the results becoming more and more self-similar downstream. Table 2 summarizes the number of grids in each direction for the current three cases.

To ensure that the current simulation results are well converged, a comparison is made on the flow profiles between current results and the coarser grids results. The coarse grids results only use 120 points in the wall normal direction. The reason that refinement is only applied in the wall normal direction is because, for wall bounded flow, the boundary layer needs to be well resolved to attain a reliable result. Figure 5 shows the U velocity and temperature profiles of case 3 at $s = 0.4$ m from two sets of grid points in the wall normal direction. These profiles look completely identical, which implies grid convergences of the current numerical simulations. To quantify the error between these two sets of grids, the infinity norm of the relative error, which is defined as the max error in the profile, is calculated. The infinity norm of relative error based on the U velocity is 2.91×10^{-5}.

In Fig. 6, the Mach number contours for blunt cones with different nose radii are shown. As the nose radius increases, the shock layer becomes thicker, and a stronger entropy layer effect can be clearly observed in the region near the leading nose for the blunter cases. The entropy layer gradually merges into the boundary layer further downstream and is eventually swallowed by the boundary layer. The appearance of an entropy layer is one of the characteristics of hypersonic flow over a blunt cone. Some studies hypothesized that the entropy layer effect would introduce a new instability mechanism into boundary-layer transition [23]. However, this new instability cannot be identified based on current LST study in this region.

The contours of the local unit Reynolds number for the three cases are shown in Fig. 7. As the nose becomes blunter, the local Reynolds number within the boundary layer is substantially reduced. As found in many previous studies, this unique pattern caused a delay in the onset of second-mode instabilities and, hence, moved the transition location further downstream. This theory has been verified experimentally on small bluntness cones [3]. However, it cannot explain the transition reversal for cones with large nose bluntness.

V. Comparison of LST and Unsteady Blowing-Suction Simulation

To validate the current LST results, unsteady simulations are carried out by imposing a wall blowing and suction perturbation at the surface of the cone with the LST-predicted unstable frequencies. This method has been used by many researchers to generate a vorticity disturbance without introducing extra mass flux into the flow [24,25]. The surface blowing and suction is applied by specifying the perturbations to the wall normal velocities in the following form:

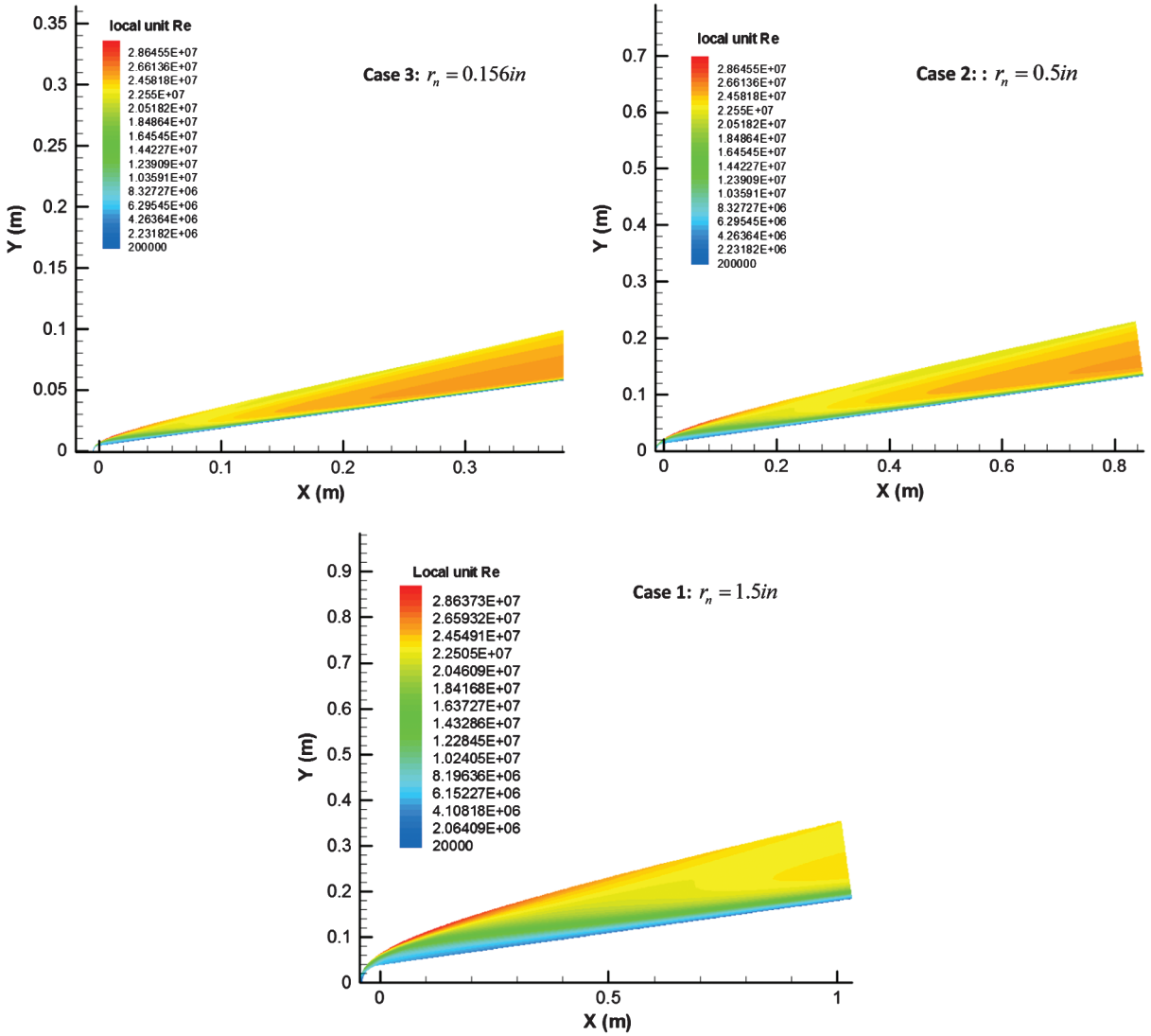

Fig. 7 Contours of the local unit Reynolds numbers for the base flows with different nose radii.

$$v_{n,\text{wall}}(x,t) = \varepsilon \sin[\alpha_w(x - x_0)] \times \sum_{n=1}^{N} A_n \cos(\omega_n t + \phi_n) \qquad (x_0 < x < x_1) \tag{10}$$

To make comparisons with the linear stability results, the disturbance amplitude is set small enough to ensure that the growth of instabilities is within the linear regime. For the current simulation, ε is set to 1×10^{-5}. The blowing and suction simulation is performed on the case of 0.156 in. nose radius cone. Instead of using a single unstable frequency, 15 equally distributed frequencies ranging from 52.55 kHz to 797.05 kHz are imposed, encompassing the unstable second-mode frequencies predicted by LST calculation. Because the perturbation amplitude is linear, multiple frequencies can be easily separated by Fourier decomposition. The blowing and suction slot is placed at $s = 0.33$ m. The disturbance waves are introduced into the steady mean flow downstream of the blowing and suction slot. Figure 8 presents the contours of the tangential velocity disturbance wave at 744.5 kHz after the Fourier decomposition. A clear periodic wave pattern can be observed in these contours as the wave propagates downstream.

From the flowfield decomposed by temporal Fourier analysis, each fixed-frequency disturbance can be represented by Eq. (11), where q' is the placeholder of any flow disturbance quantity, ω is the angular frequency of the disturbance, and ϕ is the phase angle of the disturbance. Also, the disturbance growth rate and wave number can be derived from Eq. (12) and (13), respectively. In the results presented later on, the disturbance growth rate and wave number are calculated based on the pressure disturbance along the cone surface. The nondimensional phase speed is obtained using Eq. (4), whereas the wave number was also obtained from the pressure disturbance along the cone surface.

$$q'(x,y,t) = \Re\{|q'(x,y)| \exp(i[-\omega t + \phi(x,y)])\} \tag{11}$$

$$\alpha_i = -\frac{1}{|q'|}\frac{\mathrm{d}|q'|}{\mathrm{d}s} \tag{12}$$

$$\alpha_r = \frac{\mathrm{d}\phi}{\mathrm{d}s} \tag{13}$$

If the flow perturbations of the simulation results in a local region of the boundary layer are dominated by a single wave mode, the growth rate (α_i), the wave number (α_r), and wave speed (a) computed by Eqs. (12), (13), and (4) are smooth functions of s. On the other hand, if the simulation results contain simultaneously multiple wave modes in a local region of the boundary layer, the results do not represent the wave number, growth rate, and wave speed of a single wave mode. Instead, these parameters represent a modulation of two or more wave modes. As a result, the wave number, growth rate, and wave speed along the surface direction will be oscillatory. In this case, further decomposition of different wave components is

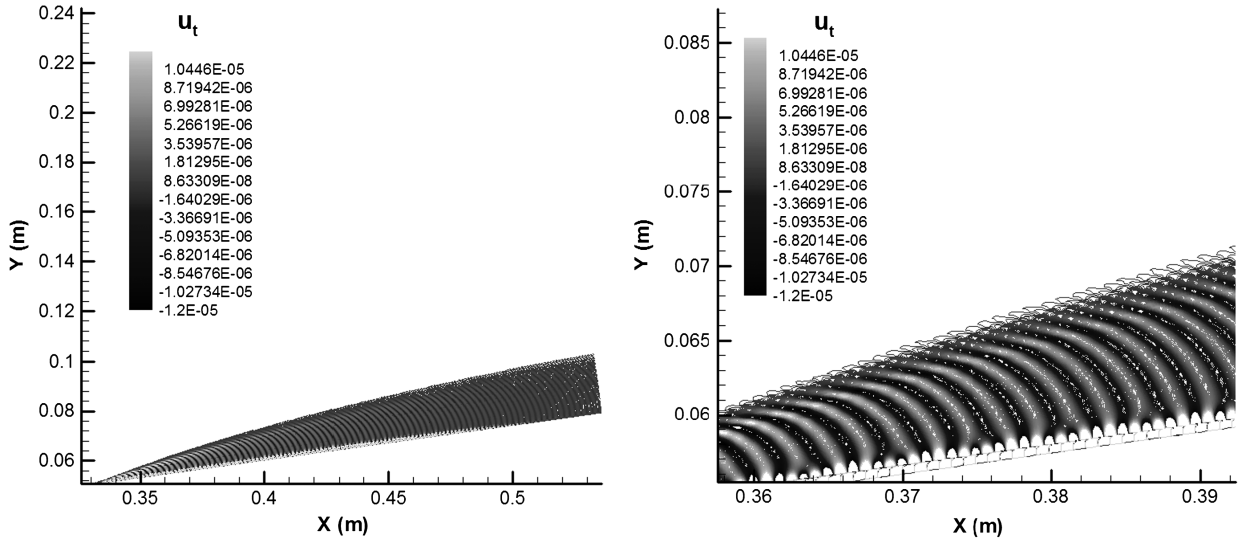

Fig. 8 Contours of tangential velocity disturbance in the unsteady simulation with frequency of 744.5 kHz for the case $R_n = 0.156$ in.

required in order to obtain the growth rates and wave numbers of the individual wave modes.

In Fig. 9, the nondimensional wave speed along the cone surface obtained from both the unsteady numerical simulation and the fast mode (F) from LST analysis at the same frequency of 774.5 kHz are shown. The early portion of the wave speed curve matches up with the LST prediction very well. However, the oscillation started around $s = 0.45$ m, indicating that this mode has not become dominant, and subsequently jumps to another mode further downstream. At $s = 0.55$ m, a new mode becomes dominant with a substantially higher wave speed. This mode is also identified by Zhong and Ma [12] in their LST analysis of a different test case. They named this the mode II, which is another stable mode excited inside the boundary layer in the later region. In addition, this figure implies that the partially excited mode in the early region is the mode F. Even though the LST predicts that, at this particular frequency, the unstable second mode should appear at this location, the excited wave mode appears to be stable due to the strong influence of the forcing blowing-suction mechanism and the existence of multiple stable modes that have not been damped out [26]. Details on mode analysis will be discussed in the next section. Here, the comparison is solely to demonstrate how the LST result can be correlated to unsteady numerical simulation.

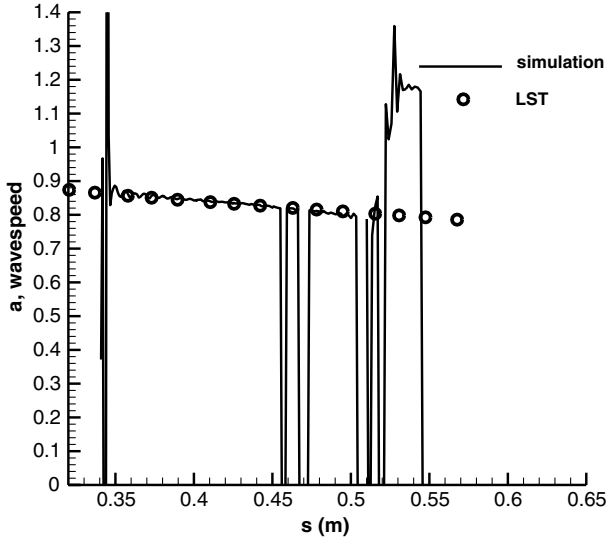

Fig. 9 Comparison of nondimensional wave numbers from direct numerical simulation (DNS) and LST with the disturbance frequency of 744.5 kHz for the case $R_n = 0.156$ in.

The mode structures from simulation and LST are also compared to verify that the LST-predicted mode is captured by numerical simulation. Figure 10 shows the excited mode in the blowing-suction simulation in comparison with the normal modes, both fast and slow, from the LST analysis at the location $s = 0.44$ m. The excited mode in simulation agrees well with the mode F from LST. It also further justifies the statement made earlier that the dominant mode excited inside the boundary layer is mode F.

To further verify how well the LST calculations predict the unstable second mode inside the boundary layer, another blowing and suction simulation is conducted further downstream to avoid the strong influence from the blowing and suction slot. In the blowing and suction simulation further downstream with a slightly different set of frequencies, substantial growths of disturbance waves at certain frequencies are clearly observed. Figure 11 shows the growths of amplitude of the pressure disturbances along the cone surface, which are set to 1×10^{-5} in the magnitude initially, for the highest five frequencies imposed in the simulation. It can be seen that the disturbance wave at 656.8 kHz is growing exponentially at this location. A similar behavior is found for the disturbance wave at 606.4 kHz. For other frequencies, the wave amplitudes either grow slowly or decay rapidly. For the other 10 waves at lower frequency, the disturbance amplitudes are all decaying.

Figure 12 shows the wave structure of a single wave frequency from the simulation in comparison to the mode S and mode F structures from the LST calculation at the location $s = 0.57$ m. The mode shapes of mode F and mode S look very similar in the location close to the surface but gradually deviate from each other as they move toward the edge of the boundary layer. In the figure, the edge of the boundary layer is located around $Y_n = 0.006$. Similar to the preceding discussion, the excited mode in the simulation is consistent with the mode F wave structure from the LST. The only difference here is that, at the specific frequency presented, mode F is actually the unstable second mode. The magnitude of mode S is scaled up for comparison purposes. In the simulation, the magnitude of mode S is several orders smaller than the one of mode F and continues to decrease as it propagates downstream.

Figure 13 shows that, for the disturbance wave at the frequency of 656.8 kHz, the wave speed from simulation and LST agree very well. However, the LST-predicted growth rate is about 10% lower than is observed from simulation. In most cases, it is hard to match the result of simulation and the LST exactly because the simulation result contains multiple excited modes. The only condition for which those two results can be well compared is when the instability completely dominates other stable modes. This condition typically occurs at the location where the instability is sufficiently far away from the forcing waves. In such cases, the stable modes will more likely decay to negligible levels compared with the unstable mode. In addition, the

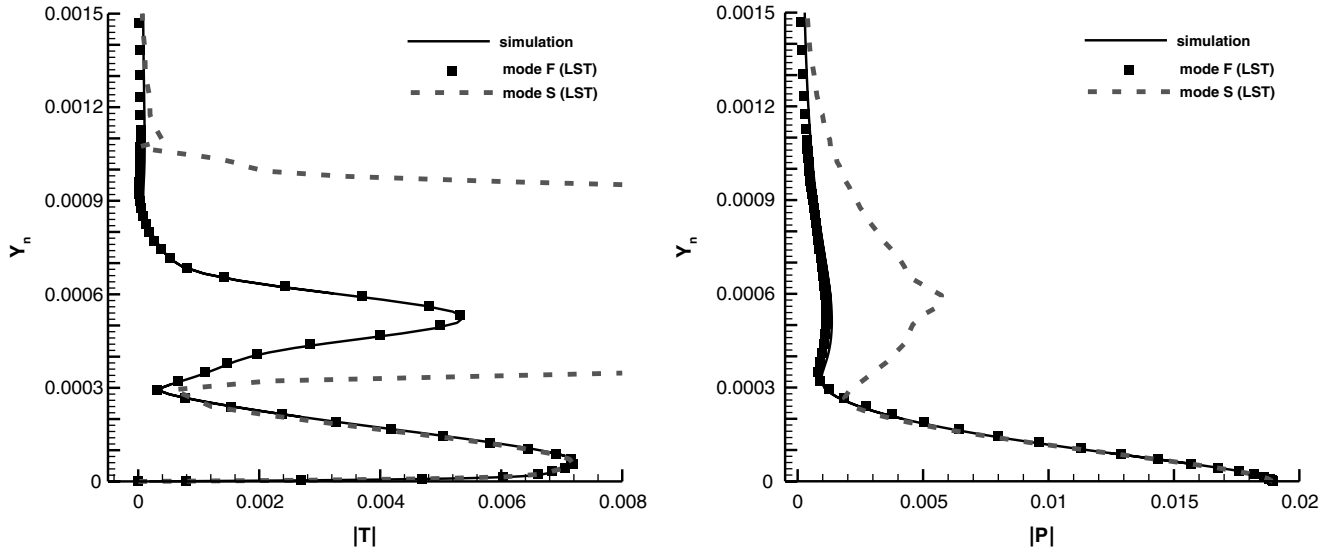

Fig. 10 Comparison of mode structures between DNS and LST at the disturbance frequency of 744.5 kHz for the case $R_n = 0.156$ in. at $s = 0.44$ m.

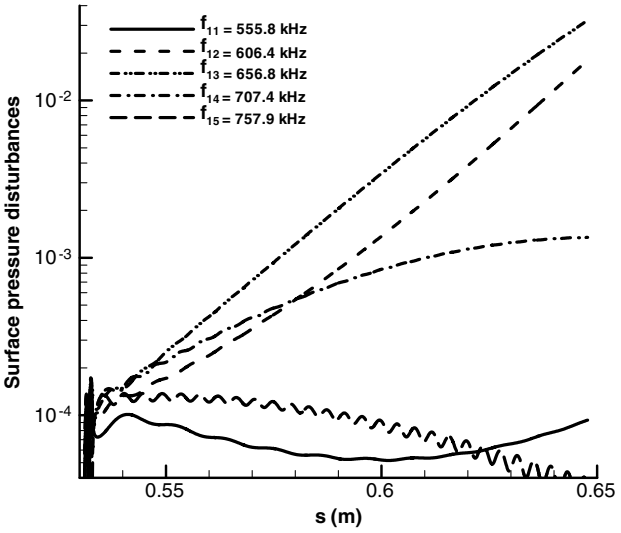

Fig. 11 Pressure disturbance amplitudes (in log-scale) along the surface for five selected frequencies.

discrepancy in growth rates can probably be attributed to the nonparallel effect of the flow within the boundary layer, which is not accounted for in the current LST model [27]. Overall, LST analysis is proven to be a reliable tool in the calculation of small amplitude instabilities in the hypersonic boundary layers. Also, LST analysis and blowing-suction simulation show consistent results in predicting the unstable second-mode behavior.

VI. Linear Stability Results

From the base flow data obtained by the numerical simulation, the instabilities for all three cases with different nose radii are successfully calculated using LST. For the base flows calculations, the cone surface temperature is set at constant room temperature, creating a cooling effect to the flow at the cone surface. According to the theoretical study by Mack [17], the wall cooling effect stabilizes the first-mode instability and destabilizes the second mode. In the current study, no first-mode instability is found for axisymmetric waves in all three test cases. Therefore, only the second-mode instability is calculated. The LST results presented are calculated by restretching the base flow profile with 121 points in the wall normal direction. The current LST code applies a multidomain approach so that we can cluster more grid points to the location where the flow variables' gradients are high. This approach substantially reduces the

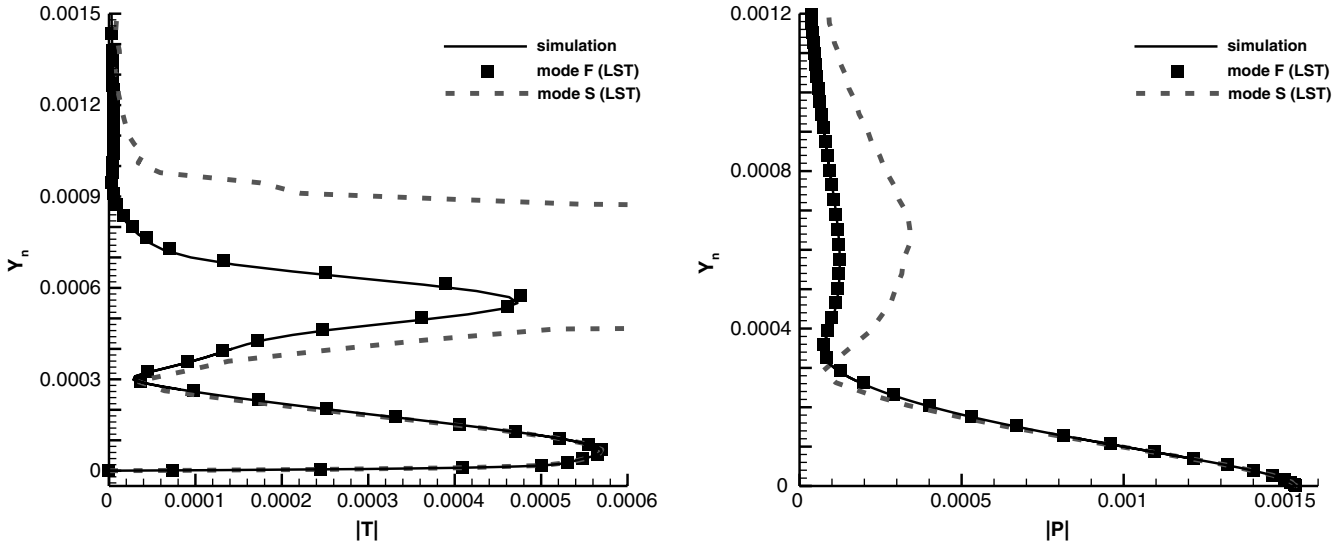

Fig. 12 Comparison of mode structures between DNS and LST at the disturbance frequency of 656.8 kHz for the case $R_n = 0.156$ in. at $s = 0.57$ m.

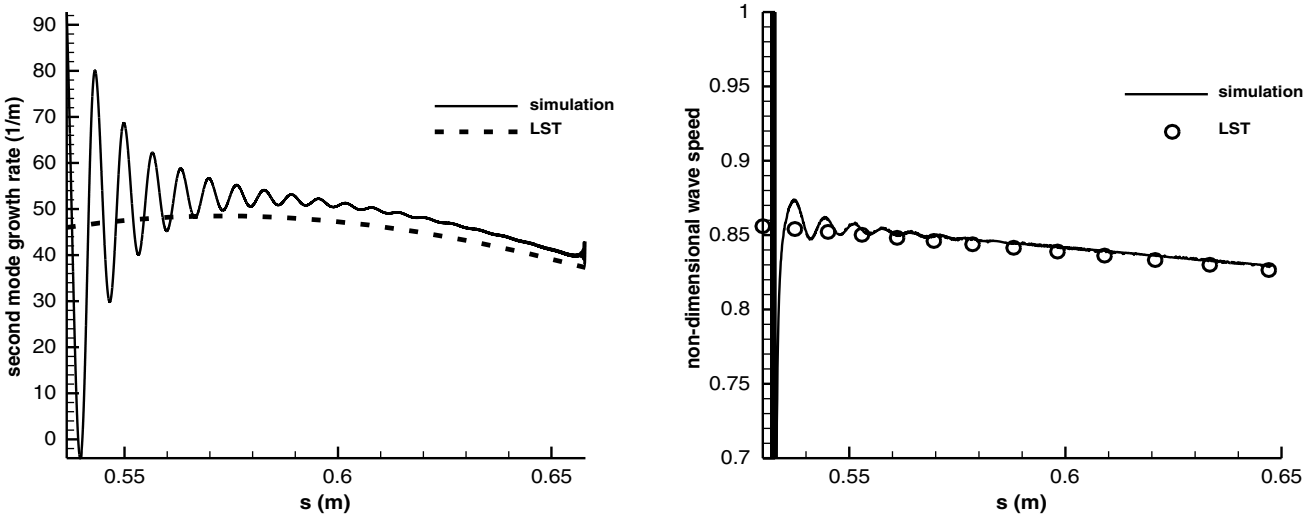

Fig. 13 Comparison of second-mode growth rate and wave speed at $F = 656.8$ kHz.

number of grid points needed in the LST calculation. To check the numerical accuracy of the LST results, a comparison is made on the growth rates at a fixed frequency of 656.8 kHz in case 3 for two sets of grid points in Fig. 14. The comparison shows that the growth rates from the current grid and the refined grid are completely identical, which implies the current grid is adequate to obtain credible LST results.

Figure 15 shows the second-mode neutral stability curves for each case. The neutral curve of the 1.5 in. case looks less smooth when compared with the other two cases. This is due to the fact that fewer data points (frequencies) are taken for this particular case. However, the general shape will not change with more points added. In this figure, it is observed that the unstable second-mode spectrum falls into very different frequency ranges for cones of different nose bluntness. Also, as nose bluntness increases, the onset of second-mode instabilities moves downstream accordingly. In the actual experiments, the locations of the onset of instability were not reported; therefore, it is hard to confirm if the transition is triggered by the same instability mechanism as predicted by LST. But, as shown in the figure, no reversal is found on the onset of instability locations. In the authors' opinion, to have a reversal in transition, a similar pattern in the onset of instability should be observed.

The second-mode dimensional growth rates versus the distance along the surface of the blunt cone are presented in Fig. 16 for the three cases with different nose radii. Some common characteristics are observed in all of these cases. First, the disturbances at higher frequencies become unstable at locations closer to the nose. Second, as the frequency decreases, the maximum second-mode growth rate becomes higher. Some trends are also found among these three cases. As the nose bluntness increases, the onset of the second-mode instability moves downstream. The range of unstable mode frequency keeps shifting to the lower end and becomes narrower as the nose becomes blunter. The frequency ranges shifting to lower values can be explained by the increase of boundary-layer thickness due to blunting the nose, which causes the wavelengths of unstable modes to become longer. The growth rates for the blunter cone are substantially lower than those of the sharper cone. Also, for the blunter case, the instability of a fixed frequency tends to grow for a longer distance to compensate for the lower growth rate it has.

The normal modes interaction is also discussed in this paper. Figure 17 shows the nondimensional wave speeds and growth rates of both mode F and mode S in the case with a nose radius of 0.156 in. for the disturbance frequency of 656.8 kHz only. In the nondimensional growth rates plot, the negative value indicates that the mode is unstable. By correlating with the wave speeds figure, it is found that the unstable second mode is excited from mode F. Mode F is defined as a discrete normal mode coming out of a fast acoustic wave that has a nondimensional wave speed of $1 + 1/M$. Traditionally, M is the Mach number at the edge of boundary layer. Because the Mach number along the edge of boundary layer changes

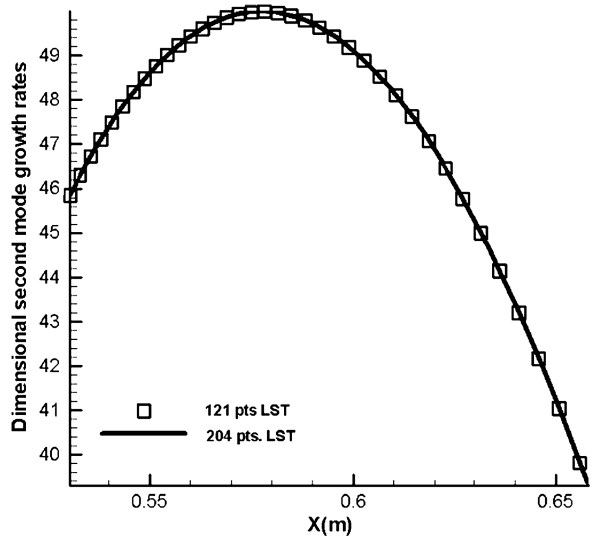

Fig. 14 Dimensional growth rates at $F = 656.8$ kHz calculated with different numbers of grid points.

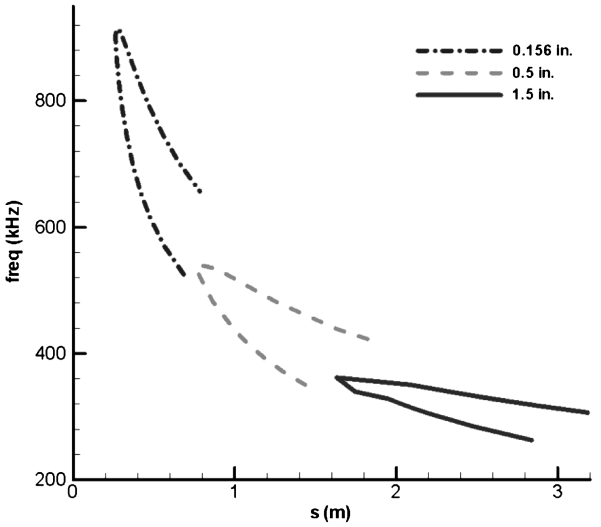

Fig. 15 Second-mode neutral stability curve for cones with three different nose radii.

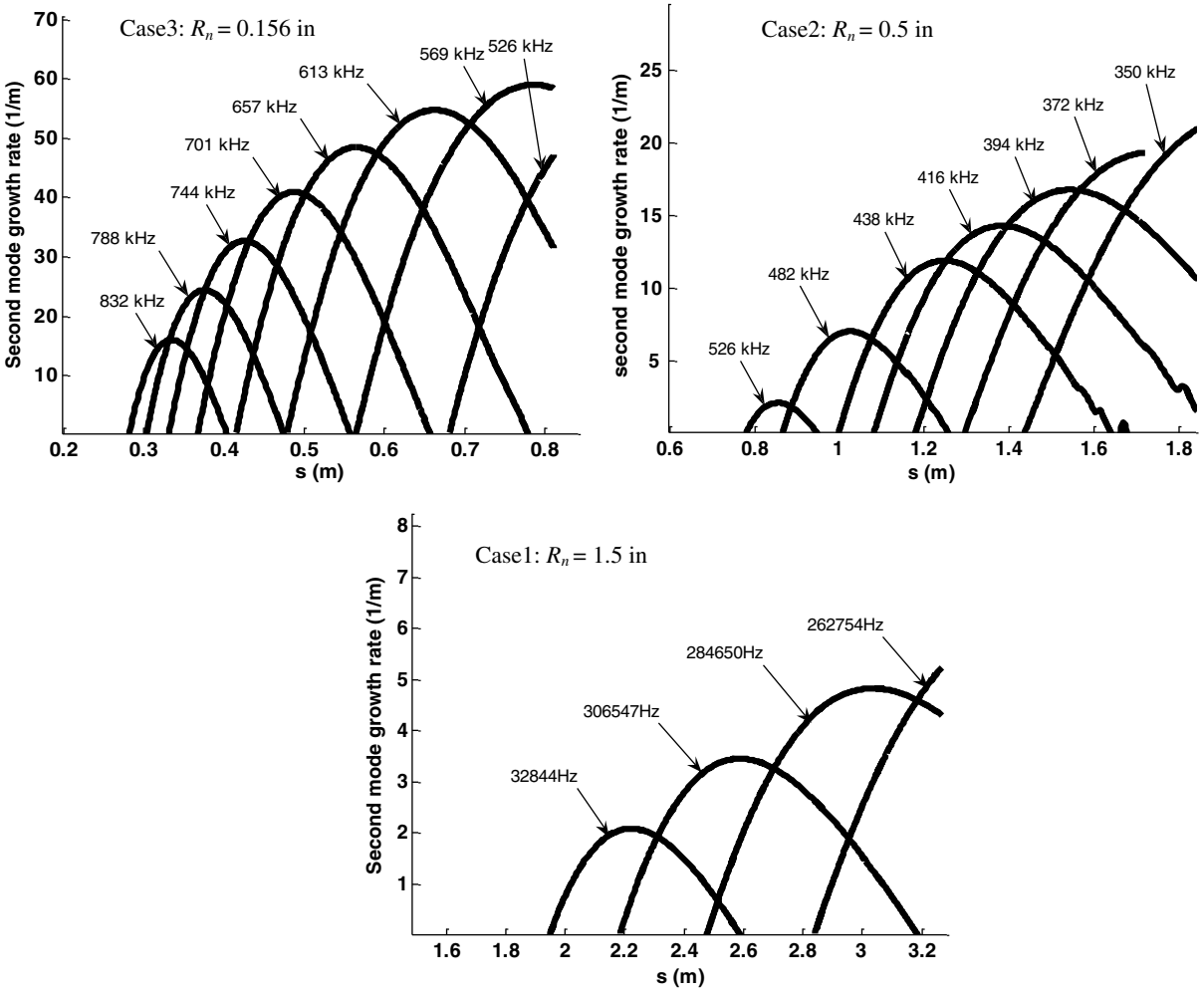

Fig. 16 Second-mode dimensional growth rates for the three cases with different nose radii.

constantly for hypersonic flow over a blunt cone, the freestream Mach number is used to keep that wave speed constant, as shown in Fig. 17 (left). Similarly, the slow acoustic wave has a nondimensional wave speed of $1 - 1/M$. In Fig. 17, both mode F and mode S are plotted to demonstrate a phenomenon called synchronization. Synchronization is a resonance between two normal modes of identical frequency when they have the same wave speed and frequency. For the disturbance at this specific frequency, the synchronization occurs around 0.42 m. Even though other studies [28,29] typically show mode S as the unstable second mode, our current cases show mode F becoming the unstable second mode. This switch can be explained theoretically due to the relatively cool wall surface temperature in the simulation [30].

The wave speeds and growth rates figures for a fixed frequency share many similarities with those at a fixed location with varying frequency. In Fig. 18, the wave speeds and growth rates versus the nondimensional angular frequency at a fixed location, $s = 0.42$ m, are plotted. These figures are very similar to Fig. 17, especially around the synchronization point. The synchronization process provides a channel for energy exchange between two normal modes, which allows transfer of energy from the stable mode to the unstable mode. Reflecting in the growth rates figure, a sudden change in

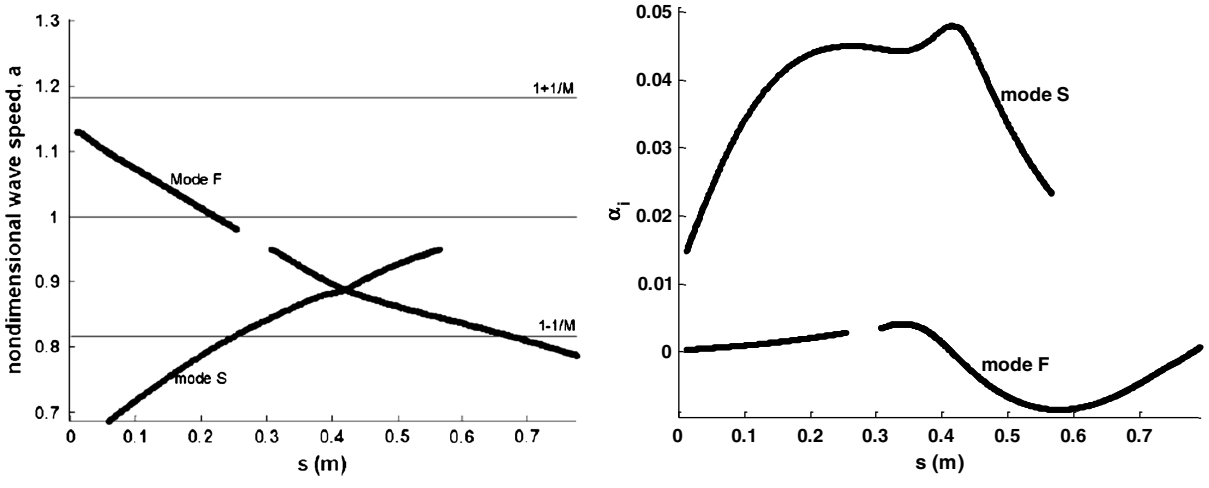

Fig. 17 LST second-mode wave speed (L) and nondimensional growth rates (R) with the disturbance frequency of 656.8 kHz for the case $R_n = 0.156$ in.

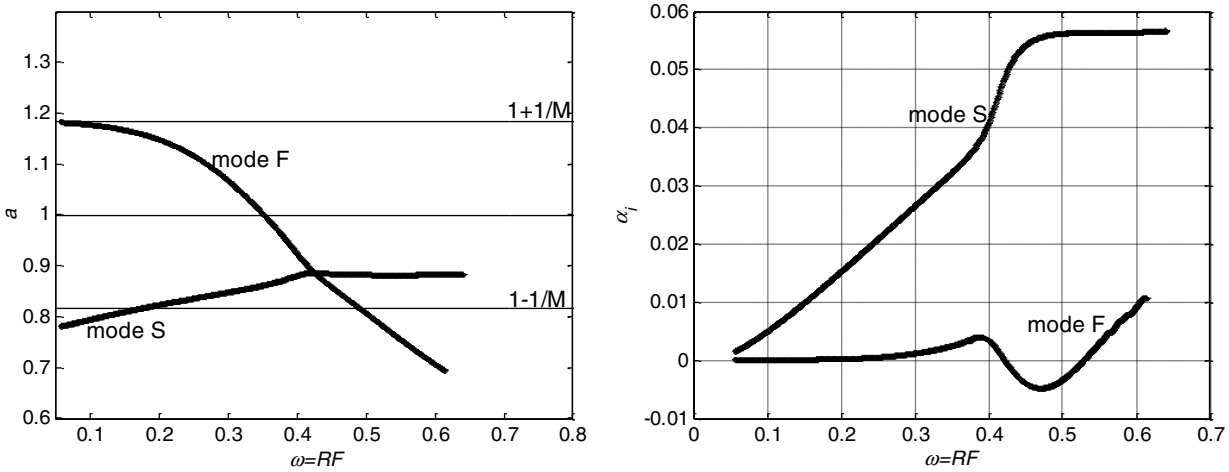

Fig. 18 LST second-mode wave speed (L) and nondimensional growth rates (R) at location $s = 0.41$ m for the case $R_n = 0.156$ in.

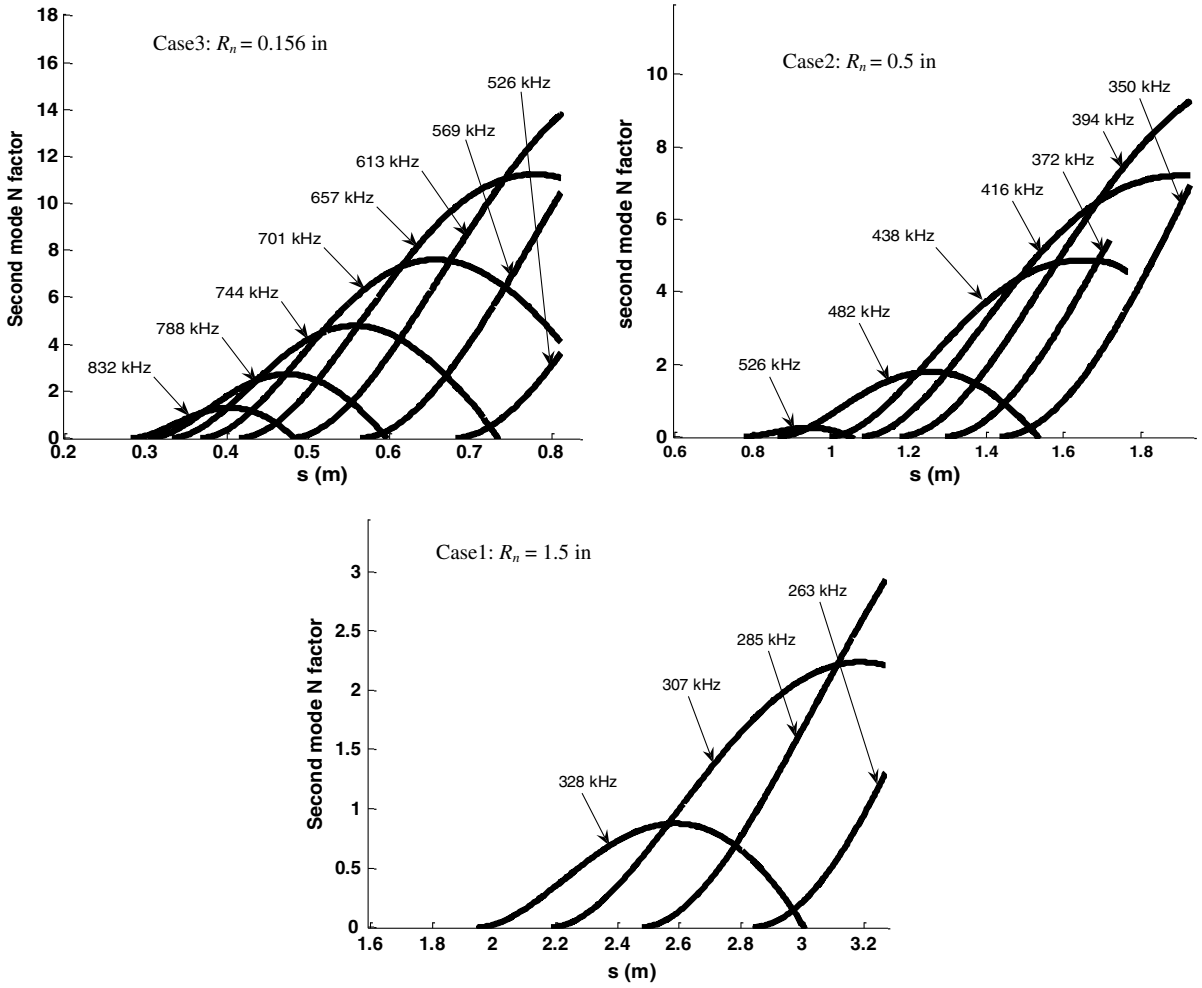

Fig. 19 Second-mode *N* factors for the three cases with different nose radii.

growth rates is observed between the two modes with an increase in the growth rate of the unstable mode and a decrease in the growth rate of the stable mode. A clear energy exchange is observed at a synchronization point between mode S and mode F in both fixed-frequency and fixed-location figures.

With the second-mode growth rates calculated, the *N* factors can be obtained by integrating the dimensional growth rates along the cone surface. In Fig. 19, the second-mode *N* factors for the three cases of different nose bluntness are presented. The *N*-factor calculations show that the sharper cone actually has much higher *N* factors than the blunter cones. In the current study, the *N* factors of the 0.156 in. blunt cone reach 16 at $s = 0.8$ m, whereas, on the other end, the 1.5 in. blunt cone only has an *N* factor about 3 at $s = 3.2$ m.

By comparing the current LST results to the experimental transition data reported by Stetson [3], disagreements are found between LST-predicted transition locations and experimentally observed transition locations. For the two cases of 0.5 in. and 1.5 in. nose radius, the experiment showed transitions occurred at 0.421 m and 0.243 m, whereas no second-mode instabilities were found at these locations according to the LST analysis. Traditionally, the *N* factor for transition is between 5 and 10. Taking an *N* factor equal to 10 as the transition prediction criteria, LST predicts that the

Table 3 Comparison of LST and experimental results

Nose radius	Freestream *Re* based on nose radius	Experimental transition location	*N* factor based on transition data	Instability onset location based on LST
0.156 in.	75,213	0.406 m	2.3	0.3 m
0.5 in.	240,665	0.421 m	N/A	0.8 m
1.5 in.	721,995	0.243 m	N/A	1.7 m

transitions occur at 0.7 m and 1.9 m for case 3 and case 2, respectively. For case 1, the *N*-factor calculation does not show a substantially large growth up to 3.2 m from the nose, which is not likely to become transition unless the initial disturbance level is very high. In Table 3, the experimental measurements and LST results are summarized.

VII. Conclusions

Stetson and Rushton's Mach 5.5 experiment [1] conducted in 1967 in which the actual reversals in transition were reported is investigated using LST technique, and the results are verified by unsteady blowing and suction simulations. The ranges of second-mode instability frequency for blunt cones with nose radii of 0.156, 0.5, and 1.5 in. are identified by LST. Because of the cool wall temperature condition being used to simulate the steady mean flows, mode F becomes the unstable second mode in the current study, which is different from some previous studies. The growth rates and *N* factors are computed for each case on selected unstable frequencies. According to the LST calculations, no reversal in the onset of the second-mode instability is observed. Because the onset locations of instability waves were not measured in the experiment, no comparisons can be made to verify that the reversal in experiments were caused by the second-mode instability waves. For the two blunter cases in which the transition reversal was observed experimentally the *N* factors based upon the second-mode instability are not large enough to initiate the laminar-turbulent transition at the locations where the actual transitions were observed experimentally. In particular, the second-mode *N* factor for the case of 1.5 in. nose radius is too weak to be the dominant mechanism for the transition. Because the experiments were conducted in a noisy tunnel environment, there is likelihood that the reversal is caused by some uncontrollable noises with the amplitude large enough that the growths of disturbances bypass the linear region and force the transition to occur earlier. However, this hypothesis cannot be justified based on the LST analysis. Hence, it is necessary to further study the nonlinear effect (finite disturbance amplitude effect) on transition to gain a more complete understanding of transition reversal.

Acknowledgments

This work was sponsored by the Air Force Office of Scientific Research (AFOSR)/NASA National Center for Hypersonic Laminar-Turbulent Transition Research and by the AFOSR/United States Air Force under Grant FA9550-07-1-0414 monitored by John Schmisseur. It was also supported by the AFOSR Small Business Technology Transfer Program phase I grant monitored by Jonathan Poggie at the Air Force Research Library at Dayton, Ohio, and John Schmisseur at AFOSR. The views and conclusions contained herein are those of the authors and should not be interpreted as necessarily representing the official policies or endorsements, either expressed or implied, of the AFOSR or U.S. Government.

References

[1] Stetson, K. F., and Rushton, G. H., "Shock Tunnel Investigation of Boundary-Layer Transition at $M = 5.5$," *AIAA Journal*, Vol. 5, No. 5, 1967, pp. 899–906. doi:10.2514/3.4098

[2] Softley, E. J., "Transition of the Hypersonic Boundary Layer on a Cone: Part II—Experiments at Mach 10 and More on Blunt Cone Transition," in GE Space Science Lab," R68SD14. 1968.

[3] Stetson, K. F., "Nosetip Bluntness Effects on Cone Frustum Boundary Layer Transition in Hypersonic Flow," AIAA paper 1983-1763, 1983.

[4] Malik, M. R., Spall, R. E., and Chang, C. L., "Effect of Nose Bluntness on Boundary Layer Stability and Transition," AIAA Paper 90-0112, 1990.

[5] Stetson, K. F., Thompson, E. R., Donaldson, J. C., and Siler, L. G., "Laminar Boundary Layer Stability Experiments on a Cone at Mach 8, Part 2: Blunt Cone," AIAA paper 84-0006, 1984.

[6] Herbert, T., and Esfahanian, V., "Stability of Hypersonic Flow over a Blunt Body," AGARD Rept. CP 514, 1993, p. 28.

[7] Kufner, E., Dallmann, U., and Stilla, J., "Instability of Hypersonic Flow Past Blunt Cones—Effects of Mean Flow Variations," AIAA paper 93-2983, 1993.

[8] Kufner, E., and Dallmann, U, Entropy and Boundary Layer Instability of Hypersonic Cone Flows—Effects of Mean Flow Variations, *IUTAM Symposium on Laminar-Turbulent Transition*, Springer–Verlag, Sendai/Japan: Berlin, 1994.

[9] Rosenboom, I., Hein, S., and Dallmann, U., "Influence of Nose Bluntness on Boundary-Layer Instabilities in Hypersonic Cone Flows," AIAA Paper 99-3591, 1999.

[10] Zhong, X., "Numerical Simulation and Experimental Comparison of Hypersonic Boundary Layer Instability over a Blunt Cone," AIAA paper 2004-2244, 2004.

[11] Zhong, X., "Effect of Nose Bluntness on Hypersonic Boundary Layer Receptivity Over a Blunt Cone," AIAA paper 2005-5022, 2005.

[12] Zhong, X., and Ma, Y., "Boundary-Layer Receptivity of Mach 7.99 Flow Over a Blunt Cone to Freestream Acoustic Waves," *Journal of Fluid Mechanics*, Vol. 556, 2006, pp. 55–103. doi:10.1017/S0022112006009293

[13] Esfahanian, V., "Computation and Stability Analysis of Laminar Flow Over a Blunt Cone in Hypersonic Flow," Ph.D. Dissertation, The Ohio State University, Columbus, OH, 1991.

[14] Zhong, X., "High-Order Finite-Difference Schemes for Numerical Simulation of Hypersonic Boundary-Layer Transition," *Journal of Computational Physics*, Vol. 144, No. 2, 1998, pp. 662–709. doi:10.1006/jcph.1998.6010

[15] Ma, Y., and Zhong, X., "Receptivity to Freestream Disturbances of Mach 8 Flow Over A Sharp Wedge," *The 41st AIAA Fluid Dynamics Conference and Exhibit*, AIAA paper 2003-0788, 2003.

[16] Zhong, X., "Receptivity of Mach 6 Flow Over a Flared Cone to Freestream Disturbance," AIAA paper 2004-0253, 2004.

[17] Mack, L. M., "Boundary Layer Linear Stability Theory," AGARD Report No. 709, 1984.

[18] Wheaton, M. B., Juliano, J. T., Berridge, C. D., Chou, A., Gilbert, L. P., Casper, M. K., Steen, E. L., Schneider, P. S., and Johnson, B. H., "Instability and Transition Measurement in the Mach 6 Quiet Tunnel," AIAA paper 2009-3559, 2009.

[19] Balakumar, P., and Kegerise, M., "Receptivity of Hypersonic Boundary Layers over Straight and Flared Cones," *The 48th AIAA Aerospace Sciences Meeting and Exhibit*, AIAA paper 2010-1065, 2010.

[20] Lysenko, V., and Maslov, A., "The Effect of Cooling on Supersonic Boundary-Layer Stability," *Journal of Fluid Mechanics*, Vol. 147, 1984, pp. 39–52. doi:10.1017/S002211208400197X

[21] Malik, M. R., "Numerical Methods for Hypersonic Boundary Layer Stability," *Journal of Computational Physics* Vol. 86, No. 2, 1990, pp. 376–413. doi:10.1016/0021-9991(90)90106-B

[22] Huang, Y., and Zhong, X., "Numerical Study of Laser-Spot Effects on Boundary-Layer Receptivity for Blunt Compression-Cones in Mach-6 Freestream," AIAA paper 2010-4447, 2010.

[23] Dietz, G., Hein, S., "Entropy-Layer Instabilities Over a Blunted Flat Plate in Supersonic Flow," *Physics of Fluids*, Vol. 11, No. 1, 1999, pp. 7–9.

[24] Wang, X., and Zhong, X., "Receptivity of a Mach 8 Flow over a Sharp Wedge to Wall Blowing-Suction," AIAA paper 2005-5025, 2005.

[25] Koevary, C., Laible, A., Mayer, C., and Fasel, H., "Numerical Simulations of Controlled Transition for a Sharp Circular Cone at Mach 8," AIAA paper 2010-4598, 2010.

[26] Tumin, A., "Multimode Decomposition of Spatially Growing Perturbations in a Two-Dimensional Boundary Layer," *Physics of Fluids*, Vol. 15, No. 9, 2003, pp. 2525–2540.

[27] Tumin, A., "Nonparallel Flow Effects on Roughness-Induced Perturbations in Boundary Layers," *Journal of Spacecraft and Rockets*, Vol. 45, No. 6, 2008, pp. 1176–1184.

[28] Zhong, X., and Ma, Y., "Boundary-Layer Receptivity of Mach 7.99 Flow Over a Blunt Cone to Freestream Acoustic Waves," *Journal of Fluid Mechanics*, Vol. 556, 2006, pp. 55–103. doi:10.1017/S0022112006009293

[29] Ma, Y., and Zhong, X., "Receptivity of a Supersonic Boundary Layer over a Flat Plate. Part 1: Wave Structures and Interactions," *Journal of Fluid Mechanics*, Vol. 488, 2003, pp. 31–78. doi:10.1017/S0022112003004786

[30] Fedorov, A., "Receptivity of a high-speed boundary layer to acoustic disturbances," *Journal of Fluid Mechanics*, Vol. 491, 2003, pp. 101–129. doi:10.1017/S0022112003005263

R. Kimmel
Associate Editor